



Improving NIF 3 ω Optics via CO₂ Laser Processing

The sustained performance of high-peak-power lasers in the National Ignition Facility (NIF) is limited by the damage of optical components that comprise the laser chain. The damage initiates in small size, on the order of tens of microns, and depends on the peak fluence of the laser. The growth of the damage is exponential in number of shots and can create excessive scatter and beam modulation. Replacing the damaged optics is an option for sustained performance of the laser system, but this option is very expensive. Therefore, a method to retard or eliminate the growth of the damage sites is needed. A method to reduce or eliminate the number of sites that initiate damage is also desirable. Optics made of fused silica are essential for conditioning the NIF laser beams and delivering these beams to the target. These optics suffer from weakened areas that are prone to damage at the laser fluences contemplated in the NIF laser systems. Damage can occur especially at the wavelength of 0.355 μm , often referred to as 3 ω . There are two options that would enable continued use of the NIF 3 ω optics. One option is to stop the growth of the damage sites before they can create excessive scatter and beam modulation. The other option is to prevent the occurrence of damage initiation.

We have recently developed a CO₂ laser spot-mitigation process that can retard or eliminate the growth of preinitiated damage sites in fused silica optics upon continued laser irradiation at 3 ω in high-fluence conditions. We have also demonstrated a CO₂ laser polishing process that can dramatically increase the resistance of fused silica optics to the initiation of laser-induced damage at 3 ω .

The laser-induced damage sites are hypothesized to contain any combination of detrimental materials, such as reduced silica (SiO_x) and silicon (Si), impurities (polishing compound, metal), and defective morphologies, such as rubble (shattered silica) and cracks. Consequently, removal or modification of these undesirable materials and morphologies is warranted. During the CO₂ laser processing, the 10.6- μm radiation from a CO₂ laser is absorbed within the top 10 μm of the silica surface, resulting

in rapid and local intense heating of the surface. The evaporation of fused silica would serve to smooth the morphology of the damage site as well as excavate and remove the offending foreign materials therein. Furthermore, the melting of fused silica may allow any agglomerated absorbing material to be dispersed in the media below, rendering them effectively harmless.

Figure 1 shows a heavily initiated damage site removed using the CO₂ laser spot-mitigation process. The CO₂ laser treatment leaves behind a smooth, Gaussian-shaped pit with no measurable UV fluorescence. Spot-by-spot CO₂ laser treatment of damage sites shows lifetime extensions to greater than 1000 shots at full NIF fluence.

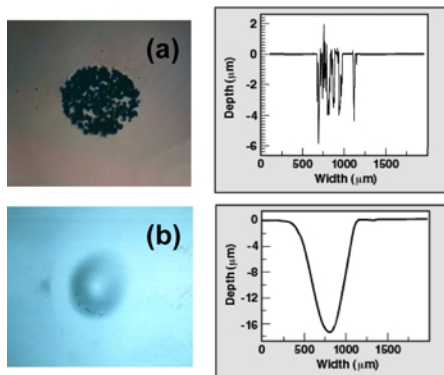


Figure 1. Damage sites in fused silica have been effectively removed using a CO₂ laser. (a) Heavily initiated damage site before CO₂ laser treatment. (b) Same damage site after 1-s exposure to 37-W defocused CO₂ laser beam.

The growth of damage in fused silica can also be mitigated without creating a substantial mitigation pit that may cause downstream problems. The CO₂ laser spot-mitigation process can arrest the growth of damage in fused silica optics by virtue of modification of the local structure of the material in the damage site. Damage growth is mitigated by elimination of cracks emanating from the initial damage site. Damage growth mitigation is also accomplished by removing sharp structures that lead to dielectric breakdown and rendering the affected area smoother.

Figure 2 shows a heavily initiated damage site that has been mitigated by localized melting using a CO₂ laser. Localized melting of damage sites by spot-by-spot CO₂ laser treatment shows

lifetime extensions to greater than 1000 shots at full NIF fluence.

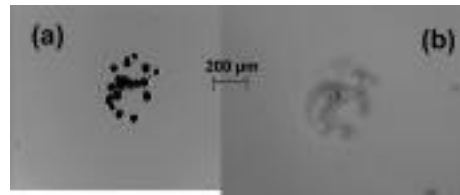


Figure 2. Damage growth in fused silica has been mitigated by localized melting of the damage site using a CO₂ laser. (a) Heavily initiated damage site before CO₂ laser treatment. (b) Same damage site after 1-s exposure to a 27-W defocused CO₂ laser.

The CO₂ laser spot-mitigation process can be automated for high-rate treatment of 3 ω optics. Damage sites would be preinitiated and then locally treated with a CO₂ laser to mitigate damage growth. CO₂ laser polishing can dramatically increase the resistance of fused silica optics to the initiation of laser-induced damage at 3 ω . The process involves treating the entire surface with a CO₂ laser prior to exposure to 3 ω . Figure 3 shows the increase in fluence threshold at which 3 ω damage in fused silica is induced. The CO₂ laser polishing process looks very promising for reducing the number of sites that initiate damage at operating fluences up to 12 J/cm². We are currently evaluating the extreme tail of the failure distribution. The combination of CO₂ laser polishing with CO₂ laser spot treatment may substantially improve NIF 3 ω optics for sustained performance at high peak power.

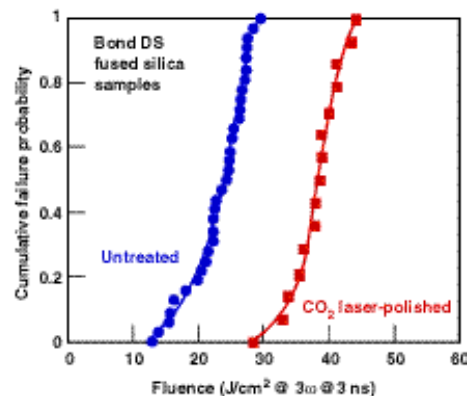


Figure 3. CO₂ laser polishing dramatically increases the resistance of fused silica to laser-induced damage at 3 ω .

—Bernie M. Penetrante



The Mercury Laser, a Diode-Pumped Solid-State Laser Driver for Inertial Fusion, Is Activated

The Mercury laser system design is based on a scalable architecture for inertial fusion with goals of achieving 10% electrical efficiency and 10-Hz operation for 100 J per 5-ns pulses. Three component technologies had to be developed for high-power, solid-state laser fusion drivers: (a) large-scale, high-performance diode lasers; (b) high-speed gas cooling of the gain media; and (c) $\text{Yb}^{3+}:\text{Sr}_5(\text{PO}_4)_3\text{F}$ (Yb:S-FAP) crystal amplifiers.



Figure 1. Mercury Laser Lab showing injection multipass filter, pump delivery hardware, and gas-cooled amplifier head.

Currently, the hardware for one complete amplifier has been delivered and is being assembled. All optics have been characterized. Three vacuum telescopes and an injection spatial filter (Figure 1) are being vacuum leak tested. The pump delivery vacuum enclosures as well as the silver-coated lens duct and homogenizer have been assembled. Two water-cooled copper backplanes have been fabricated and tested. Seventy-two diode laser tiles (each consisting of 23 bars operating at >115 W peak per bar) capable of generating a total of over 160 kW of 900-nm light have been assembled, characterized, and are undergoing integrated testing with the backplane.

The Mercury laser system has been designed to avert damage and to offer a scalable architecture. To avert damage, the telescope lenses are located near the relay image planes in the amplifiers to minimize beam modulation. Extensive ghost, amplified spontaneous emission (ASE), and pencil

beam analysis guided the current architecture and set constraints on optical quality, surface reflectivity, and wedge angles, as well as the extinction required of a Pockels cell in the reverser. The high-average-power Pockels cell is composed of an identical pair of KD*P crystals with their axes oriented such that the thermal birefringence cancels (Figure 2).

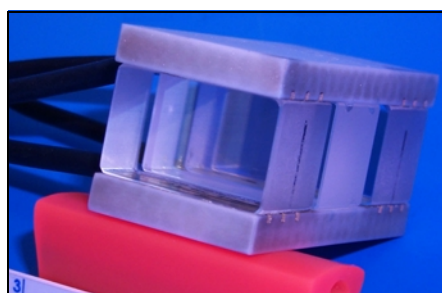


Figure 2. A half-aperture (1.5 × 2.5 cm) high-average-power Pockels cell.

Recent breakthroughs have been made in the growth of the ytterbium-doped strontium fluorapatite (S-FAP) amplifier crystals. Crystals with large areas free of defects allow 1/2 scale slabs to be diffusion-bonded together to achieve full-scale amplifier slabs at Litton Airtron (Figure 3) and LLNL (Figure 4).

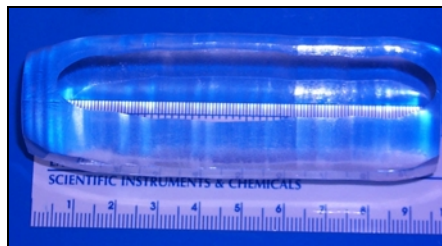


Figure 3. Litton Airtron boule is currently being fabricated into subslabs necessary for a full-size diffusion-bonded slab (4 × 6 × 0.75 cm).

These Czochralski-grown crystals have been challenged by defects including cracking, cloudiness, bubble core defects, grain boundaries, anomalous absorption, and crystal inclusions. These defects are essentially under control, although further fine-tuning is needed to assure reproducibility.

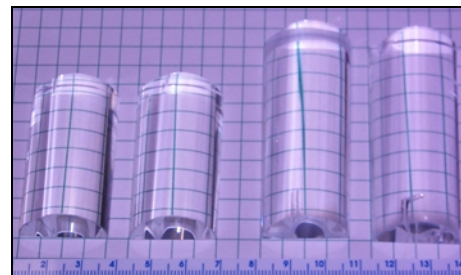


Figure 4. Polished LLNL boules showing clarity. Boules are currently being fabricated into Mercury slabs.

High-speed gas cooling allows operation at 10 Hz while maintaining wavefront quality for a 5-diffraction-limited beam. A diagram of the gas-cooling system is shown in Figure 5, along with interferometry results using surrogate Nd:glass slabs showing $<1/16$ wavefront distortion induced by the gas flow.

Near-term experiments include characterization of the diode backplanes and integrated beam propagation experiments in April. One of the goals for FY01 is the demonstration of the half Mercury system, including architecture, diodes, gas cooling, and material enough for seven full-aperture S-FAP amplifiers.

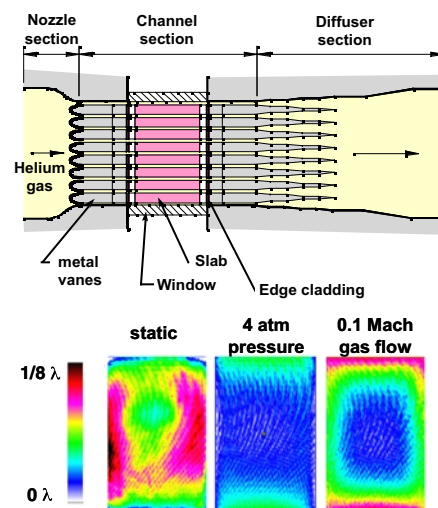


Figure 5. Wavefront distortions through the gas-cooled amplifier head showing wavefront distortion for static, differential pressurized, and differential flow conditions.

—Andy Bayramian & Camille Bibeau



Laser Science & Technology

Dr. Lloyd A. Hackel, Program Leader

UCRL-TB-136126-01-11

42-kW Diode Array Delivered to the HELSTF Program

Under the support of the U.S. Army's Space and Missile Defense Command, LS&T recently completed the fabrication of a 42-kW-peak-power laser-diode array for pumping of high-average-power solid-state heat-capacity

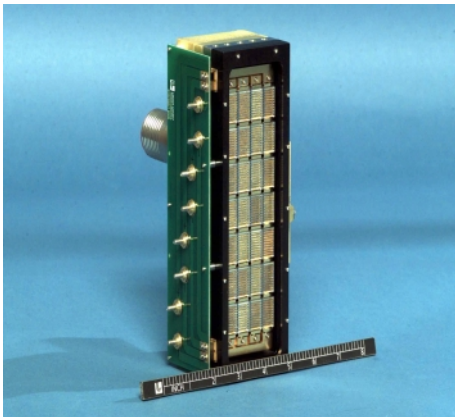


Figure 1. A 100 kW-class diode array module developed for pumping of high-average-power solid-state lasers.

laser for applications in tactical short-range air defense missions. Figure 1 shows the laser-diode module, which is constructed from 280 edge-emitting laser-diodes mounted on a backplane packaged by 28 closely packed **Silicon Monolithic Microchannels** tiles (SiMMs) arranged in 4×7 configuration. This pump module is designed to deliver 42 kW of 808-nm radiation when operated at 200 Hz or higher duty cycles.

The production of high-average-power by laser-diode arrays on the scale demonstrated here has relied on the development of a silicon-based diode packaging technology that has been actively pursued at LLNL for the last 15 years. The silicon package that serves to cool the laser-diode bars is produced by photolithography and etching techniques used in the microelectronic industry. Using this technology, we were able to manufacture thousands of miniscule 30- μm -wide channels in silicon substrates. Water flowing through these microchannels effectively cools the laser diode bars, which are

mounted on the silicon at a location less than 200 μm from the channels. By mounting 10 diode bars onto a single heatsink, a 10-bar package (referenced as a tile and shown in Figure 2, top photograph) can be easily assembled to serve as a unit cell from which larger 2D diode arrays can be built up through tiling. Noteworthy in this design is that the brightness of the array is extremely high (presently $1 \text{ kW}/\text{cm}^2$ at a 10% duty factor), due to the compact tiling of the heatsinks and the precision placement of 10-element microlens arrays on each tile. The microchannel cooling technique allows higher duty factor operation if required by future systems.

Over the years, we have developed several types of diode packaging technologies for high-power applications. Special considerations were given to both the ease of fabrication and power scalability. In the current SiMMs design, we were able to preserve the same effective heat removal capability that characterized our original rack-and-stack silicon microchannel-cooled package by incorporating microchannels into the silicon directly below the attached laser-diode bars.

In order to fully utilize the light emitted from laser-diode bars (particularly along the fast axis that has a 30° divergence angle), we have also designed microlenses to collect radiation along the fast axis. A single-step microlens-mounting technique was developed to eliminate the production steps necessary to individually attach microlenses to each diode bar, dramatically reducing package cost. To achieve good optical performance, microlenses must be placed with a positional tolerance of a few microns relative to the diode bar emitter facets, and individual diode bars within a tile must also be positioned relative to one another with at least this same few-micron accuracy.

Using a V-groove technology on the front surface of the package accomplishes precision placement of the laser-diode bars. V-grooves are generated using the same etching technology that is used to fabricate the microchannels in silicon and serve as pads to which the laser diode bars are attached and precisely registered. Because the V-grooves are defined lithographically, output facets of individual bars can be located with micron precision relative to one another over the entire

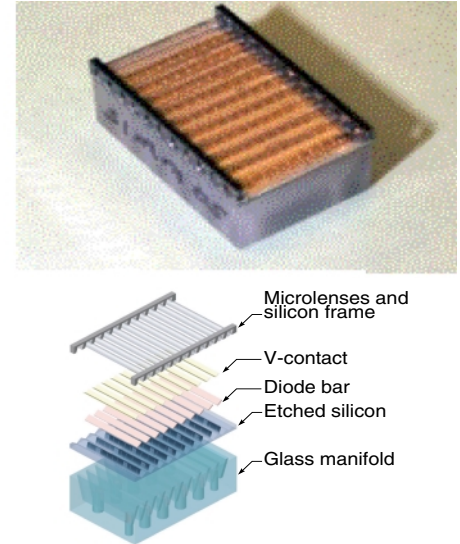


Figure 2. The SiMMs package. Top: Photograph of an individual SiMMs package. Bottom: Assembly drawing showing the various SiMMs package components in an exploded view. The V-grooves on the front surface of the silicon enable us to precisely position the laser-diode bars and microlenses with micron precision.

SiMMs tile. Single-step microlens mounting is accomplished using precision frames fabricated in the form of silicon runners. Lenses are preloaded and glued into these silicon runners forming a ladder-like structure consisting of 10 lenses as shown in Figure 2. These microlenses have effectively reduced the beam divergence of the array to <1 degree.

Using diode bars procured from the Coherent Semiconductor Group, Santa Clara, CA, we successfully achieved 1.5 kW of output power from a single tile (10-bar SiMMs package) with wall plug efficiencies approaching 50%. We plan to optimize the optical performance of the 42-kW array module and demonstrate pumping of Nd:GGG slab laser in future experiments. The SiMMs package represents a breakthrough in high-power diode-array packaging technology enabling us to scale the output of 2D diode arrays to 100 kW or larger with extremely high brightness.

—Ray Beach and Barry Freitas



Laser Science & Technology

Dr. Lloyd A. Hackel, Program Leader

UCRL-TB-136126-01-04

IMPROVING ANTIREFLECTION COATINGS FOR NIF KDP AND DKDP OPTICS

Antireflection (AR) coatings are required to minimize reflection losses from the fused silica windows, lenses, and the potassium dihydrogen phosphate (KDP) and deuterated KDP (DKDP) switch and conversion crystals on the National Ignition Facility (NIF) laser. Porous sol-gel coatings, first developed for Nova laser optics, have been used on many high-power laser systems such as OMEGA, Helen, Phebus, and Beamlet. These sol-gel coatings are composed of layers of 10- to 20-nm-diam silica spheres that form a film with approximately 50% porosity. The resultant film has an index of refraction of 1.2, approaching the theoretical optimum index for a single-layer AR coating on fused silica or KDP. Figure 1 shows the coating performance.

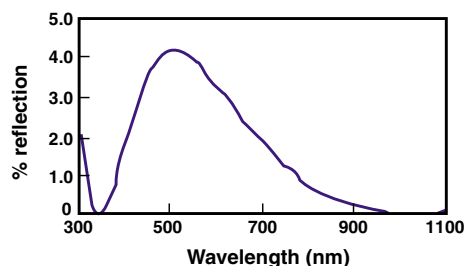


Figure 1: Reflection from the surface of a porous sol-gel coating on KDP, optimized for 1053-nm laser light.

Porous sol-gel coatings are the only AR coatings that have demonstrated survivability at projected 351-nm operating fluences for NIF. Unfortunately, the porosity that gives these films their outstanding optical and damage performance also makes them extremely sensitive to their use environment. As the pores adsorb organic or water vapor from their environment, the films' index of refraction increases and they lose their antireflection properties. For coated KDP optics, exposure to humidity has a second detrimental impact—it produced etch pits like those shown in Figure 2. These pits scatter laser light, causing both additional loss of energy on target and the potential for increased laser damage to downstream optics. Etch pits, which were first

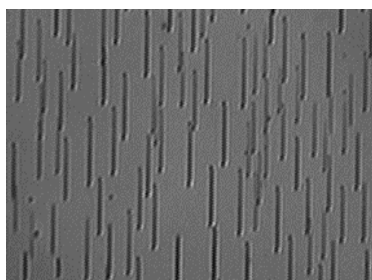


Figure 2: Etch pits on a Beamlet third-harmonic-generation crystal.

observed during the final Beamlet campaigns, motivated an effort to identify and implement “etch-pit mitigation” methods for NIF crystals.

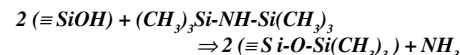
Surface adsorption of water vapor, subsequent capillary condensation of water into the porous sol film, and the dissolution of the underlying substrate cause etch-pit formation on optics under humid environments. During the past few years, we have developed several methods to effectively retard etch-pit formation on optical crystals: (1) application of a polymer barrier coating, (2) chemical passivation of the KDP surface, and (3) modification of the surface chemistry of sol-gel to eliminate capillary condensation.

The first method, applying a barrier coating of methyl silicone polymer to reduce etch-pits formation, hence improving the optical performance of KDP frequency conversion crystals, was used in the '90s in Nova experiments. This silicone coating process is now used on the OMEGA conversion crystals and will be used in NIF on frequency conversion crystals.

The second method was developed to protect the KDP crystals used for optical switching. Methyl silicone coatings would be oxidized and destroyed by the oxygen plasma in the NIF Pockels cells. We developed a thermal annealing process that produces a 70-nm-thick, water-insoluble, dehydrated-phosphate layer on the surface of finished KDP optics. During the annealing process (three months at 160°C), the KH_2PO_4 molecules on the optic surfaces undergo interfacial dehydration reaction and produce a polymeric film with composition of Kurrol's salt $(\text{KPO}_3)_n$. We were able to monitor the development of this chemical passivation

layer by Fourier transform infrared (FT-IR) spectroscopy, electron spectroscopy for chemical analysis (ESCA), and x-ray diffraction.

The deuterated third-harmonic-generation crystal (DKDP) cannot tolerate the temperatures required for either the thermal annealing process or the Nova methyl silicone process. To prevent etch-pit formation on the DKDP, we have modified the surface chemistry of the sol-gel particles themselves, converting them from a hydrophilic (water-loving) to a hydrophobic (water-hating) surface, as shown in Figure 3. During the surface treatment process, the hydrophilic surface silanols (Si-OH) are reacted with hexamethyldisilazane (HMDS) to produce hydrophobic trimethylsilyl groups:



We were able to control the stability of the hydrophobic surface by optimizing concentration of reactive surface silanol groups prior to introduction of the HMDS. One unexpected benefit of the hydrophobic surface modification is that it appears to reduce the sol's affinity for polar organic contaminants as well as water.

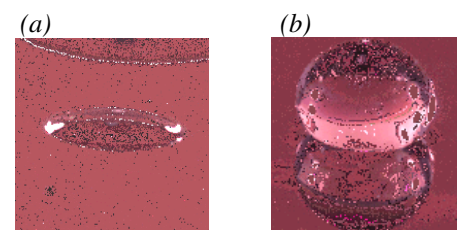


Figure 3: Water droplet on a (a) hydrophilic and (b) hydrophobic porous sol-gel coating.

To date, all three methods—methyl silicone, thermal annealing, and hydrophobic sol—have prevented etch-pit formation on KDP and DKDP surfaces exposed to 75% relative humidity for over six months. This provides the flexibility to match the etch-pit mitigation method to the use environment and optical requirements for each NIF crystal type.

Future work will focus on the interaction of laser energy with these coatings to ensure their survivability at projected NIF operating fluences.

—Pamela Whitman



Laser Science & Technology

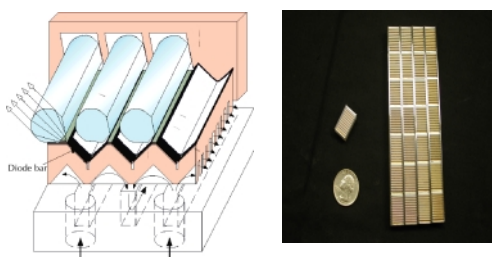
Dr. Lloyd A. Hackel, Program Leader

UCRL-TB-136126-01-05

DEVELOPMENT OF HIGH-POWER, MICROCHANNEL-COOLED, LASER-DIODE ARRAYS IS UNDER WAY

Under the support of the U.S. Army's Space and Missile Defense Command and in collaboration with industrial partners (Raytheon, Litton Airtron, and others), we are developing high-average-power (100-kW-class), diode-pumped solid-state, heat-capacity laser technology for applications in tactical short-range air defense missions. To establish a solid technical basis for the 100-kW laser, we are building a testbed utilizing a neodymium-doped gadolinium gallium garnet (Nd:GGG) slab as laser media (with an active region of $5 \times 10 \text{ cm}^2$, a third of the ultimate 100-kW system) and four arrays of microchannel-cooled laser diodes as pump source.

The figures below show a schematic drawing of a silicon monolithic microchannel-cooled (SiMM) laser-diode array and a diode array package. These SiMM packages are similar to those developed for the Mercury laser project (see LS&T Program Update, September 2000), but contain only 10 diode bars instead of 23. Each array package contains 28 SiMM "tiles" arranged in a 4×7 configuration.

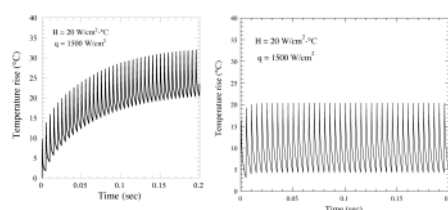


Schematic of a microchannel-cooled laser-diode array and a picture of a 4×7 diode array and individual "tile."

One of the distinguishing features of the SiMM package is its ability to rapidly conduct heat away from the active region of the diode. This special feature is of particular importance to the Army's High-Energy Laser Systems Test Facility (HELSTF) applications because the laser is required to turn on rapidly and stay on at full power during the multisecond target engagement period. Long waiting period for thermal equilibrium is not an option for this application.

Furthermore, if the temperature rise is too large, the laser wavelength might shift out of the absorption band (diode emission shift $\sim 0.3 \text{ nm}/^\circ\text{C}$) and result in laser power loss.

To better understand the thermal behavior of the SiMM package, we performed a series of heat-conduction calculations. For comparison, we also analyzed the performance of a commercial system with a copper-based heatsink. The results of these modeling calculations are shown in the following figures.



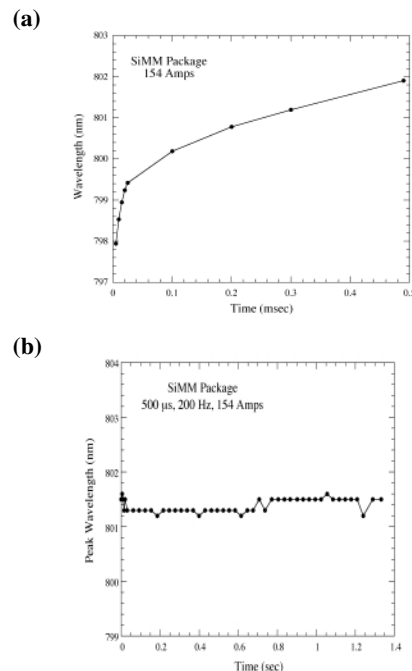
Plots display the temporal behavior of diode temperature (in the active region) calculated for a thermal input of $1.5 \text{ kW}/\text{cm}^2$, 500- μs pulse duration at 200 Hz.

As shown in the charts, the SiMM package appears to have lower thermal impedance and shorter thermal equilibration time. The smaller thermal mass of the monolithic cooler allows the diodes to reach equilibrium much more quickly than the more massive copper heatsink. As a result, one would expect very little change in the time-integrated spectrum for the SiMM package over the duration of the excitation (10 seconds). However, the smaller thermal mass of the monolithic cooler could also cause greater temperature oscillation during each individual pulse and hence result in a larger intrapulse wavelength shift.

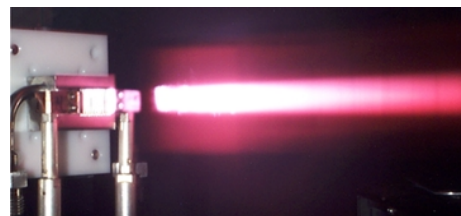
To verify this model, we measured the intrapulse as well as the long-term (time-integrated) spectrum of the diode light collected from a 10-bar SiMM package operated at 150 W/bar. We see in chart (a) that the rapid temperature rise during the 500- μs excitation pulse results in an intrapulse wavelength shift of about 4 nm, which is much narrower than the absorption bandwidth (10 nm) of Nd:GGG material.

We also measured the long-term wavelength stability of the diode array operated

at a 200-Hz repetition rate and 10% duty cycle. As can be seen in chart (b), the wavelength varies very little ($<0.5 \text{ nm}$) during the course of the burst, indicating very little long-term temperature increase, in good agreement with the model.



In recent tests, steady operation of a SiMM laser-diode array at $1.5 \text{ kW}/\text{cm}^2$ was successfully demonstrated with the 10-bar package (150 W/bar); see photo below. Output power degradation was found to be less than 3.4% after 5×10^7 pulses at 10% duty factor. We plan to test the Nd:GGG-slab testbed in the near future to optimize pump efficiency. We will also optimize the design of the SiMM package to further reduce costs of production.



The 10-bar SiMM package in operation

—M. Rotter and B. Freitas



Laser Science & Technology

Dr. Lloyd A. Hackel, Program Leader

UCRL-TB-136126-01-06

CONTINUOUS MELTING PROCESS PRODUCES HIGH-QUALITY, METER-SIZED GLASS SLABS

A novel, continuous melting process is being used to manufacture meter-sized slabs of laser glass (Figure 1) at a rate 20 times faster, five times cheaper, and two to three times better optical quality than with the previous one-at-a-time, "discontinuous" technology process. The glasses manufactured by this new process are Nd-doped phosphate-based glasses and are marketed as LG-770 (Schott Glass Technologies) and LHG-8 (Hoya Corporation USA). After *finishing*, these amplifier slabs will serve as the gain media on the National Ignition Facility (NIF) and the Laser Megajoule (LMJ) lasers. The combined NIF and LMJ lasers require approximately 75 times the laser glass production capacity used for Nova and OMEGA with glass-part sizes more than two times larger. Thus, almost 8000 laser glass plates will be needed for the two laser systems: this represents a volume in excess of 125 m³ (330 metric tons) of finished optical quality glass.

Discontinuous processing methods have been used with good results for producing small quantities of laser glass. However, the discontinuous process has a small throughput and a single melting system can, at best, only produce fewer than five glass plates per week. In addition, the quality of the glass produced can vary from one melt to the next simply because of small, but random, run-to-run variations in processing conditions. Continuous glass melting, on the other hand, has two major advantages: much greater production rates can be achieved, and once steady state is achieved, there is little if any measurable variation in glass properties from one glass plate to the next. Continuous optical glass melting systems are generally divided into several interconnected zones. Each zone consists of one or more vessels designed



Figure 1. Continuous strip of laser glass coming out of coarse annealing at Hoya Corporation.

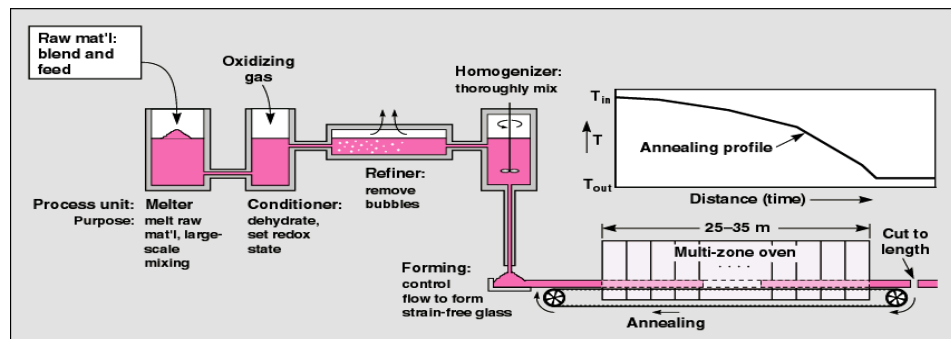


Figure 2. Schematic representation of the continuous laser glass melting systems.

to carry out a particular part of the process. In laser glass continuous melters, there are six main interconnected processing zones (Figure 2): (1) raw material mixing and feeding, (2) melting, (3) conditioning, (4) refining, (5) homogenizing, and (6) continuous strip forming.

The manufacture of laser glass by continuous melting is a result of numerous technical advances after a six-year, joint research and development effort between LLNL, Hoya, and Schott:

1. *Pt-inclusion removal*: Microscopic Pt particles (<10 μm) in the laser glass can absorb laser light and cause fracture in the glass (laser-induced damage). Research on their formation and dissolution has led to a redox-controlled process for minimizing the number and size of inclusions in the glass.

2. *OH removal*: Hydroxyl (OH) groups in the glass quench the fluorescence of the Nd and reduce the laser output energy. Research on the chemical mechanism of OH removal (dehydroxylation) using reactive gas bubbling and the incorporation of this information in process models have led to a 50 times reduction of OH content in continuously melted glass. Figure 3 illustrates the dramatic improvements in glass OH content that have been achieved.

3. *Fracture prevention*: Phosphate laser glasses are prone to fracture due to their low fracture toughness and high thermal expansion. Finite elemental heat transport and stress analyses combined with the identification of various stress sources and research in crack growth have led to improvements in the annealing process to eliminate fracturing.

4. *Impurity minimization*: Metal ion impurities (such as Fe²⁺ and Cu²⁺) at 10 parts-per-million level can increase the optical absorption of the glass above acceptable limits. New analytical techniques

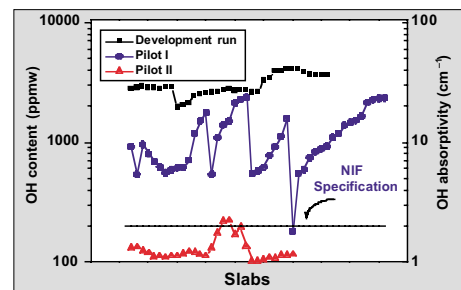


Figure 3. OH content (in ppmw and OH absorptivity) in randomly selected laser glass slabs showing the nearly 50x reduction in this contaminant achieved during a recent melt campaign.

to quantify impurity levels combined with research on the absorption characteristics of these impurities have led to much improved specifications and quality control procedures for both the laser glass and the raw materials.

5. *Homogeneity*: Laser glass requires a refractive index uniformity (i.e., optical homogeneity) of about one-part-per-million, requiring advanced forming technologies.

6. *Quality assurance*: A number of unique quality-assurance tools have been developed to inspect large optical glass plates at a high rate. These tools include large-aperture (24-inch) phase-measuring interferometers and large-aperture laser damage testers.

The recent melting campaigns have been very successful yielding a combined output of ~3400 NIF/LMJ-quality slab blanks to date. The LLNL Laser Glass Group will continue their effort to further improve glass yield in future campaigns.

—Tayyab Suratwala, Jack Campbell



Laser Science & Technology

Dr. Lloyd A. Hackel, Program Leader

UCRL-TB-136126-01-07

NEW WET-ETCHING PROCESS FIGURES LARGE-APERTURE AND ULTRATHIN OPTICS

With support from the Laboratory Directed Research and Development (LDRD) Program, LS&T has recently developed a low-cost wet-etching tool for precision optical figuring and finishing of large-aperture and ultrathin optical components (see Figure 1). This wet-etch figuring (WEF) method uses applicator geometry and surface tension gradients (the Marangoni effect) to confine the footprint of the flowing etchant on the surface. In contrast to the conventional methods using abrasive slurries or ion milling, no mechanical or thermal stresses or residues are applied to the optic by this process. WEF also uses a real-time interferometry to measure the thickness of the optical material while surfacing and figuring, which then controls the placement and dwell time of the wetted zone.

Traditionally, small-tool finishing or figuring of optical surfaces has involved moving a small, abrasive polishing tool in a controlled manner to shape the surface of an optic. Recent advances in finishing involve flowing jets of fine abrasive slurries, magneto-rheological control of the viscosity of abrasive slurry, or the use of ion-beam milling. All of the above-mentioned techniques rely on calibrated removal rates and are, therefore, iterative processes: the workpiece must be dismounted from the machine and measured, reworked and remeasured, until specifications are met. These polishing techniques cannot easily be used to figure thin optics since the local mechanical stresses involved cause workpiece deformations that impact removal control and can even cause breakage.



Figure 1. LLNL-developed wet-etching tool (operated by authors).

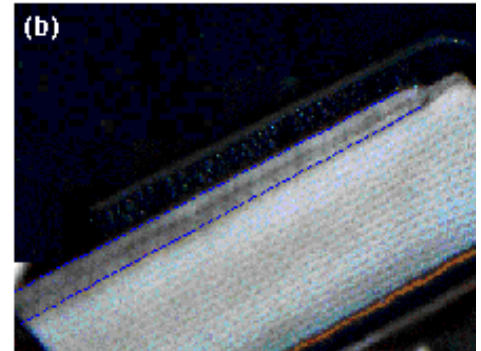
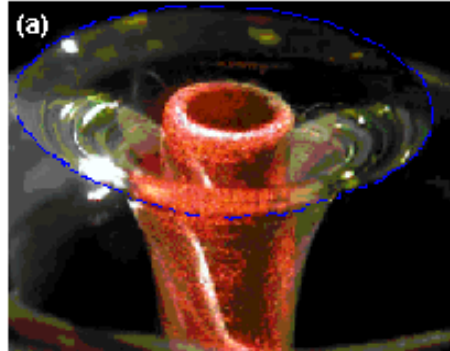


Figure 2. (a) Looking downwards through the thin glass being processed, left is a drop of etchant solution ~10 mm in diameter adhering to the underside of a glass sheet. The solution is flowing up through and then down the outside of the tube. (b) A 150- x 10-mm rectangular wetted zone in which liquid flows up out of a slit and down the inclined plane on either side. In both cases, a blue line has been drawn on the three-phase contact line as a visual aid.

We have employed the Marangoni effect to confine the wetted zone of a hydrofluoric acid etchant on the surface of an optic. Figure 2 shows circular and linear etching toolheads developed for two- and one-dimensional (2- and 1-D) figuring. For the case of a circular toolhead, the wetted zone size can be controlled between ~1 to 10 cm by flow pulsation and wicking. The width of the wetted zone for 1-D figuring can be similarly controlled, and the length can be made arbitrarily large. An interferometer that measures the local glass thickness from above is used in feedback control for closed-loop figuring.

We have made several custom phase correction and beam-shaping optics using the 2-D WEF tool. An example is shown in Figure 3. We are presently constructing a 1-D WEF machine that will take the 1-D thickness ripple out of commercially extruded, 850- x 1150- x 0.7-mm glass sheets.

We have also fabricated static wavefront correctors for high-power laser application. Figure 4 shows an 80-mm-aperture corrective optics recently fabricated for the Atomic Weapons Establishment (AWE), U.K., Helen laser, based on specifications given by AWE researchers. The optic is to be installed upstream in the laser chain to precorrect for wavefront aberrations due to amplifiers and other optics. The optic surface contour specified by AWE requires a maximum excursion of 12 μm over this aperture. The final transmitted wavefront profile and interferogram of the 80-mm-diameter wavefront corrector are shown in Figure 3. The 380- μm -thick optic was

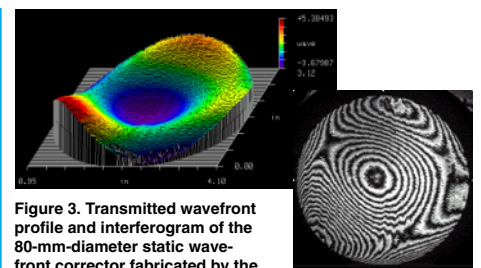


Figure 3. Transmitted wavefront profile and interferogram of the 80-mm-diameter static wavefront corrector fabricated by the WEF process. The optic is 380- μm thick.

completed within one machine setup step, using the circular 2-D WEF tool. The surface profile is within 100 nm of the target goal. The residual error of the part is equivalent to a Strehl of 0.26.

WEF is an ideal technology for the fabrication of large-aperture phase-modifying optics and optically flat optics. It is particularly useful for precision figuring of very thin ($\ll 1$ mm), lightweight optics for use in space and astronomy, and high-power laser systems in which nonlinear effects due to bulk transmissive optics need to be minimized. We will continue to improve the precision of the WEF machine and to use it to demonstrate figuring of continuous phase plate for NIF. We are also trying to form partnerships with private companies to commercialize this process.

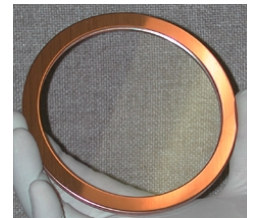


Figure 4. Photograph of finished part.

—M. Rushford and J. Britten



Laser Science & Technology

Dr. Lloyd A. Hackel, Program Leader

UCRL-TB-136126-01-08

HIGH-BANDWIDTH TECHNOLOGY FOR HIGH-POWER SHORT-PULSE LASERS

With support from the Laboratory Directed Research and Development (LDRD) Program, LS&T has recently developed a front-end technology utilizing optical parametric chirped pulse amplification (OPCPA) to replace the regenerative amplifier previously used in the Nova Petawatt laser system. This method obtained a gain of 6×10^7 with broad bandwidth without the use of electro-optic modulators or multipass amplification. Preliminary experiments have demonstrated 6% overall pump-to-signal conversion with excellent bandwidth fidelity. The wavelength and pulse energy level obtained from this OPCPA is ideal for seeding kJ-class Nd:glass amplifiers (such as the National Ignition Facility) and other high-average-power, ultrashort-pulse laser systems.

Previously high-energy lasers employing chirped pulse amplification (CPA) were built on a hybrid (Ti:sapphire-Nd:glass) laser technology. Ti:sapphire regenerative amplifiers were used as preamplifiers because of their intrinsic large gain bandwidth. One difficulty with the hybrid laser system is its low pulse contrast and generation of prepulses by the regenerative amplifier. In target experiments where focused intensities near 10^{21} W/cm² are possible, a 10^{-2} to 10^{-3} level of prepulse can significantly perturb the target prior to the arrival of the main pulse. The contributing factors to low pulse contrast include amplified spontaneous emission (ASE), leakage from regenerative amplifiers, and hard edge spectral clipping on diffraction gratings and other optical components. The gain coefficient of Ti:sapphire at 1054 nm (laser wavelength) is low, necessitating a large number of passes in the regenerative amplifier. Each time the pulse completes one round-trip in the cavity, a small fraction (~1%) leaks out of the cavity, producing prepulses spaced one cavity round-trip time ahead of the main pulse. While spectral clipping can be eliminated by using large-aperture gratings, the pulse contrast remains fundamentally limited by ASE and leakage from regenerative amplifiers. Single-pass OPCPA eliminates prepulses originating from regenerative amplifiers and reduces the ASE by approximately one order of magnitude compared to Ti:sapphire.

OPCPA offers additional advantages when

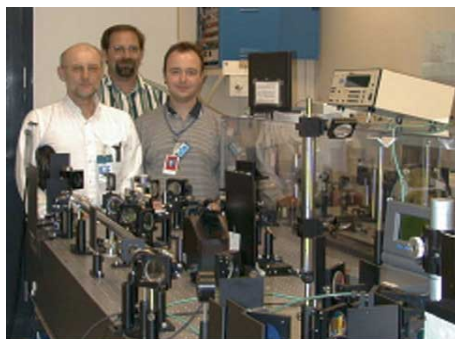


Figure 1. Optical parametric chirped pulse amplifier pumped by a commercial Q-switched Nd:YAG pump laser.

compared to regenerative chirped pulse amplification: low thermal aberration, greater wavelength flexibility, higher gain, high beam quality, and lower B-integral as a result of short beam path through the gain medium.

Figure 1 shows the compact OPCPA pumped by a commercial Q-switched Nd:YAG laser. It consists of three β -barium borate (BBO) crystals, utilizing type I angular phase matching. A commercial frequency-doubled Q-switched Nd:YAG laser is used to pump the OPCPA. The first two crystals are configured as a preamplifier and pumped by 90 mJ, while 420 mJ is used to pump the power amplifier crystal. We obtained 1.5 mJ of amplified signal from the preamplifier, which was seeded by 0.5-nJ stretched oscillator pulses. A saturated gain of 20 was obtained from the power amplifier BBO crystal, which amplifies the signal beam up to 31 mJ. A pump-to-signal conversion efficiency of 6% was achieved. This is the highest overall extraction efficiency demonstrated from an OPCPA to date. The input stretched pulse is 3 ns in length, interacting with the 8.5-ns (FWHM) pump pulse. The fraction of pump energy extracted during the temporal window defined by the seed pulse is estimated to be >20%.

Figure 2 shows the measured spectra of the stretched seed, the amplified signal from the preamplifier, and the output from the power amplifier. In these experiments, we saturate the OPCPA in order to obtain large extracted energy. The amplified signal spectrum is modified by strong saturation in the power amplifier and resembles a top-hat shape near the point of maximum conversion efficiency. The intensity

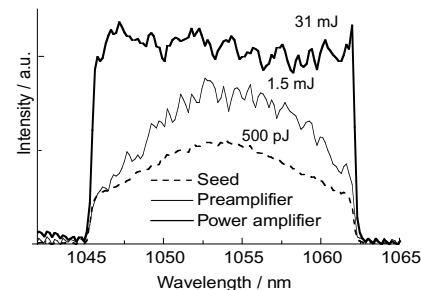


Figure 2. Seed and amplified signal spectra in OPCPA.

autocorrelation of the recompressed pulse at energy of 31 mJ is shown in Figure 3. The recompressed amplified pulse duration is measured to be 310 fs, 10% longer compared to the best-achieved seed recompression before amplification in OPCPA. The pulse width is limited by the spherical and chromatic aberrations occurring in the pulse stretcher. Our calculations show negligible self-phase modulation due to short beam path through the gain medium.

We have successfully demonstrated high gain, high conversion efficiency, and good amplified pulse beam quality ($M^2 < 2$) in OPCPA. We anticipate widespread use of OPCPA as front-end technology for glass-based Petawatt laser systems. In the future, it may be possible to exploit the full bandwidth capability of OPCPA to produce kJ-class pulses with durations of several tens of femtoseconds. This would potentially allow focused intensities of 10^{24} W/cm² or higher for experiments in the extreme field science.

—Igor Jovanovic and Brian Comaskey

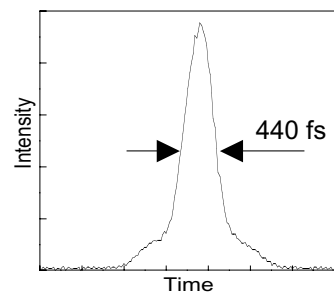


Figure 3. Autocorrelation trace of the recompressed pulse. Deconvolved FWHM pulse width is 310 fs, assuming a Gaussian pulse shape.



Laser Science & Technology

Dr. Lloyd A. Hackel, Program Leader

UCRL-TB-136126-01-09

LASER PEENING INCREASES THE CORROSION RESISTANCE OF METAL

In a joint research effort with the Yucca Mountain Project (YMP), we are evaluating laser peening (Figure 1) as a technique to

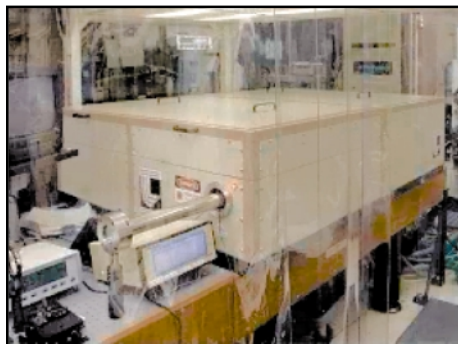


Figure 1. LLNL's LasershotSM Peening System.

improve the corrosion resistance and service lifetime of metal canisters designed for final disposal of high-level radioactive waste, dismantled reactors, and retired weapon components. Nuclear waste around the country will be stored underground at Yucca Mountain in welded canisters of Alloy 22. These canisters are required to last 10,000 years without leakage. However, the process of welding the end caps on these canisters can cause tensile stress that allows defects to grow into cracks and accelerate corrosion. Previous work (see August 2000 *LS&T Program Update*) demonstrated that laser peening can transform tensile stress into compressive stress deep into the material and prevent the growth of such cracks. In recent tests, we found that laser peening not only stops crack propagation in welds, it also retards the overall corrosion rate of metal.

By optimizing the process parameters such as laser pulse duration (10 to 30 ns), fluence intensity (50 to 300 J/cm²) and number of treatment pulses, we were able to induce compressive stress deep into the metal. Figure 2 shows the residual stresses induced by laser peening on titanium measured at various depth levels. Compressive residual stress extending to depth of several millimeters is achieved with the laser pulses at various fluence intensities.

We have conducted a number of stress-corrosion cracking (SCC) and surface corrosion experiments on 304 and 316 stainless-steel weld.

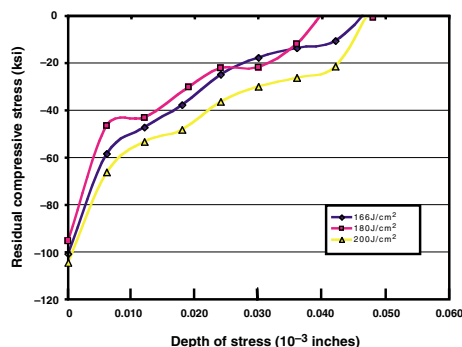


Figure 2. Laser peening induces compressive stress on titanium.

Figure 3 shows results from 304 stainless specimens bathed in 40% MgCl₂ solution at 160°C, which accelerates cracking and corrosion. On the unpeened weld, cracks perpendicular to the weld developed within 24 hours, while no observable cracks were detected on the peened weld even after weeks of exposure.

We have also assembled a high-temperature reactor to perform SCC experiments on large-size (foot-scale) test samples. Two foot-scale stainless-steel welds were tested. The first experiment was on a seam-weld made by two pieces of 12- × 5.5- × 0.5-in. 316 stainless steel. One side of the welds was laser-peened and the other side of the same weld was not. Two bottomless Erlenmeyer flasks were used to boil the MgCl₂ solution at 156°C. The unpeened weld area showed cracks and corrosion within 5 days, while the laser-peened weld area showed no signs of cracking or corrosion even after 10 days of exposure. This result is consistent with the electrochemical data obtained by French researchers earlier [P. Peyre et al., *Materials*

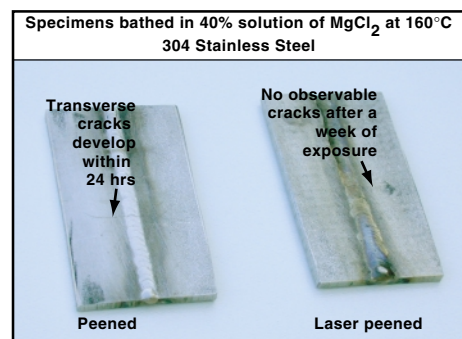


Figure 3. Laser-peened 304 stainless-steel weld on the right showed no cracking even after a week in 160°C MgCl₂ solution.

Science and Engineering, A280, 294-302, (2000)]. Laser peening appears to increase the free corrosion potential and reduce the passive current densities of metal.

The second experiment was conducted on a similar size of 316 stainless steel weld. Laser peening was performed on a selected area of the welds. A foot-scale bottomless Erlenmeyer flask was used to hold the MgCl₂ solution over both the peened and unpeened areas. After 5 days bathed in the boiling MgCl₂ solution, cracks developed on the surface at the unpeened area while the laser-peened area showed no observable cracks. Cracks originating from the unpeened area appeared to propagate, bypass, and cease at the peened zone (see Figure 4).

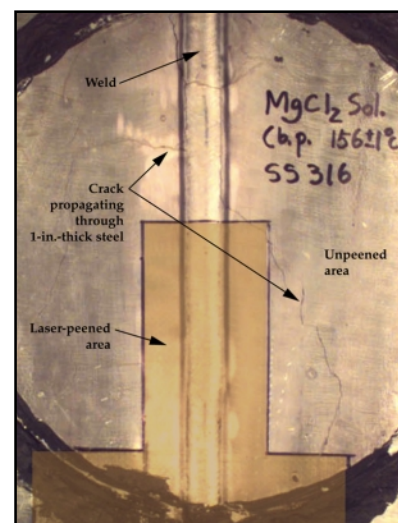


Figure 4. Laser-peened area of a welded 316 stainless steel showed no observable cracks even after 5 days in 156°C MgCl₂ solution.

Our experiments demonstrated that laser peening can significantly improve the resistance of metal to stress-corrosion cracking and surface corrosion. We are working closely with industry to commercialize this technology. Besides nuclear waste disposal, the U.S. industry could apply this technology to improve reactor safety and reliability and to extend the operational life of reactor components (internals, tubes, bolts, and pins) so that boiling-water reactors and pressurized water reactors will have a higher service life and lower operating cost.

—John Honig, John Halpin, and Francis Wang



Laser Science & Technology

Dr. Lloyd A. Hackel, Program Leader

UCRL-TB-136126-01-10

METER-SCALE GRATINGS DELIVERED TO RUTHERFORD FOR PETAWATT LASER UPGRADE

LLNL recently completed the fabrication of meter-scale diffraction gratings for Rutherford Appleton Laboratory's (RAL) Vulcan Laser Petawatt Upgrade. RAL in the United Kingdom has been operating Vulcan at 100 TW, providing sub-picosecond pulses at intensities of 10^{19} W/cm² for the study of high-intensity laser/matter interactions. The upgrade (which is based on LLNL's Petawatt laser and scheduled for completion in 2002) will enable the compression of 500-J, 500-picosecond pulses for 1 petawatt (10^{15} W) of power and 10^{21} W/cm² at target.

The enabling components for achieving this ultrahigh power density are large-aperture diffraction gratings, which are only obtainable from LLNL. These gratings are optimized for high-efficiency and flat wavefront at the nominal 1053-nm use wavelength. These gold-overcoated plane gratings are patterned in photoresist using laser interference lithography, on optically polished substrates 94 cm in diameter with the top and bottom chords removed for a vertical aperture of 75 cm. The grating pattern is written on LLNL's large holographic exposure station, which utilizes two 110-cm-diameter F6 fused silica aspheric collimating lenses to provide a flat-wavefront exposure field at this aperture. Figure 1 shows LS&T's large-aperture diffractive

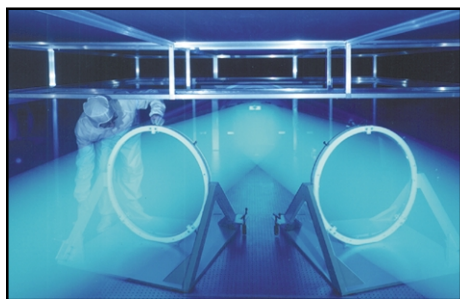


Figure 1. Large-aperture diffractive optics production chamber, where the meter-scale diffractive gratings are produced.

optics production chamber, where the meter-scale diffractive gratings are produced.

RAL has contracted with LLNL for several gratings over the years. The fabrication procedure is basically the same as that used for the original LLNL Petawatt gratings (see March 2000 *LS&T Program Update*), with the exception of recent

improvements made to the exposure system to improve fringe stability during patterning of the grating. Briefly, the substrate is cleaned and then a layer of material is vacuum-deposited as an adhesion layer for the photoresist. A film of photoresist, ~250 nm, is applied by meniscus coating, and the substrate baked in a large convection oven to dry the resist. The blank is then mounted on the large interferometer table and allowed to stabilize for at least 24 h. The grating pattern is then written by exposing the resist film to interfering plane waves of 413-nm light from a Kr-ion laser. Exposure times are typically 10 minutes. During this time, the spatial location of the fringe pattern generated at 1480 lines/mm (675-nm period) must be held to within a small fraction of this period to maintain the intensity contrast in the exposure plane. Various methods are utilized to accomplish this, including vibration isolation, isothermal environmental control, and active fringe stabilization using a portion of the two exposure beams to provide a secondary interference pattern. A fringe detection/piezoelectric mirror system is used to control the path length of one of the beams to compensate for vibration drift. Following exposure, the latent image in the photoresist film is developed by contact with a base solution to convert it into a surface relief image.

The grating structure evolution is monitored with a probe laser during development to control the details of the groove shape. Following the development step, visual inspection for defects is done, and measurements of the diffraction efficiency of the photoresist grating are made to determine the spatial uniformity of the pattern. The grating is subsequently hard-baked, and then ~500 nm of gold is applied by vacuum e-beam evaporation. The grating is then subjected to full-aperture diffraction efficiency measurements at the use wavelength as well as wavefront measurements. If at any time of the process, specifications are not met or defects in the grating surface are identified, the gold and photoresist layers can be stripped off and the grating blank reprocessed without the need to repolish.

Figure 2 shows the full-aperture diffraction efficiency of two 94- × 75-cm gold-overcoated petawatt compressor gratings (measured at 1064 nm, 54° incidence angle) that meet specifications for delivery. Also shown is the footprint of the beam RAL researchers are to compress; 80 and 90% contours are also shown. The average diffraction efficiency in the beam footprint for these gratings is 92.8% and 93.8%, respectively, which represent the best uniformity we have been

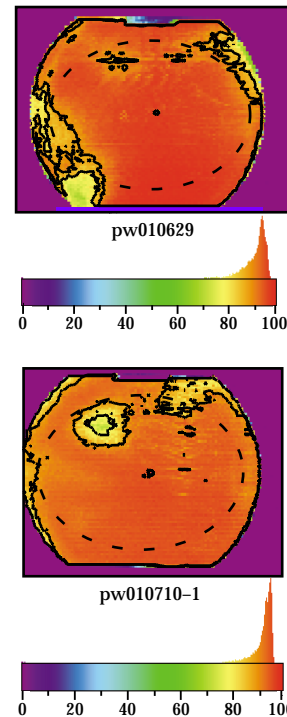


Figure 2. Full-aperture diffraction efficiency of two compressor gratings. Dashed lines show footprint of the compressed beam.

able to achieve to date at this scale. Figure 3 shows one of the gratings during wavefront testing at LLNL. The two large gratings, along with four smaller ones for the pulse stretcher and diagnostics, have been shipped to RAL.

—Jerry Britten, Leslie Summers, Carly Hoaglan, John Toeppen, and Gary Stone

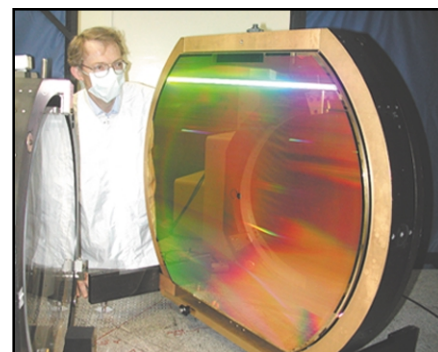


Figure 3. A meter-scale grating undergoing a wavefront test at LLNL.



Laser Science & Technology

Dr. Lloyd A. Hackel, Program Leader

UCRL-TB-136126-01-11

42-kW Diode Array Delivered to the HELSTF Program

Under the support of the U.S. Army's Space and Missile Defense Command, LS&T recently completed the fabrication of a 42-kW-peak-power laser-diode array for pumping of high-average-power solid-state heat-capacity

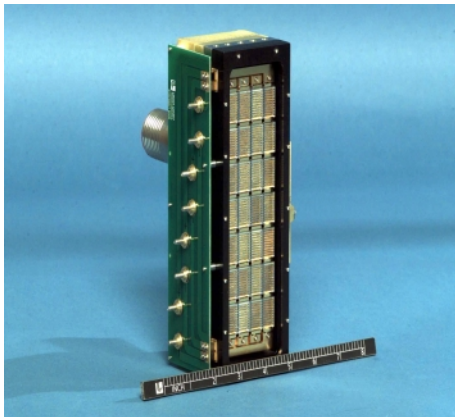


Figure 1. A 100 kW-class diode array module developed for pumping of high-average-power solid-state lasers.

laser for applications in tactical short-range air defense missions. Figure 1 shows the laser-diode module, which is constructed from 280 edge-emitting laser-diodes mounted on a backplane packaged by 28 closely packed **Silicon Monolithic Microchannels** tiles (SiMMs) arranged in 4×7 configuration. This pump module is designed to deliver 42 kW of 808-nm radiation when operated at 200 Hz or higher duty cycles.

The production of high-average-power by laser-diode arrays on the scale demonstrated here has relied on the development of a silicon-based diode packaging technology that has been actively pursued at LLNL for the last 15 years. The silicon package that serves to cool the laser-diode bars is produced by photolithography and etching techniques used in the microelectronic industry. Using this technology, we were able to manufacture thousands of miniscule 30- μm -wide channels in silicon substrates. Water flowing through these microchannels effectively cools the laser diode bars, which are

mounted on the silicon at a location less than 200 μm from the channels. By mounting 10 diode bars onto a single heatsink, a 10-bar package (referenced as a tile and shown in Figure 2, top photograph) can be easily assembled to serve as a unit cell from which larger 2D diode arrays can be built up through tiling. Noteworthy in this design is that the brightness of the array is extremely high (presently $1 \text{ kW}/\text{cm}^2$ at a 10% duty factor), due to the compact tiling of the heatsinks and the precision placement of 10-element microlens arrays on each tile. The microchannel cooling technique allows higher duty factor operation if required by future systems.

Over the years, we have developed several types of diode packaging technologies for high-power applications. Special considerations were given to both the ease of fabrication and power scalability. In the current SiMMs design, we were able to preserve the same effective heat removal capability that characterized our original rack-and-stack silicon microchannel-cooled package by incorporating microchannels into the silicon directly below the attached laser-diode bars.

In order to fully utilize the light emitted from laser-diode bars (particularly along the fast axis that has a 30° divergence angle), we have also designed microlenses to collect radiation along the fast axis. A single-step microlens-mounting technique was developed to eliminate the production steps necessary to individually attach microlenses to each diode bar, dramatically reducing package cost. To achieve good optical performance, microlenses must be placed with a positional tolerance of a few microns relative to the diode bar emitter facets, and individual diode bars within a tile must also be positioned relative to one another with at least this same few-micron accuracy.

Using a V-groove technology on the front surface of the package accomplishes precision placement of the laser-diode bars. V-grooves are generated using the same etching technology that is used to fabricate the microchannels in silicon and serve as pads to which the laser diode bars are attached and precisely registered. Because the V-grooves are defined lithographically, output facets of individual bars can be located with micron precision relative to one another over the entire

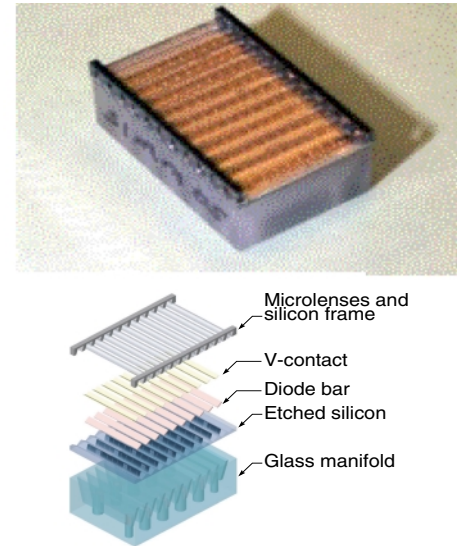


Figure 2. The SiMMs package. Top: Photograph of an individual SiMMs package. Bottom: Assembly drawing showing the various SiMMs package components in an exploded view. The V-grooves on the front surface of the silicon enable us to precisely position the laser-diode bars and microlenses with micron precision.

SiMMs tile. Single-step microlens mounting is accomplished using precision frames fabricated in the form of silicon runners. Lenses are preloaded and glued into these silicon runners forming a ladder-like structure consisting of 10 lenses as shown in Figure 2. These microlenses have effectively reduced the beam divergence of the array to <1 degree.

Using diode bars procured from the Coherent Semiconductor Group, Santa Clara, CA, we successfully achieved 1.5 kW of output power from a single tile (10-bar SiMMs package) with wall plug efficiencies approaching 50%. We plan to optimize the optical performance of the 42-kW array module and demonstrate pumping of Nd:GGG slab laser in future experiments. The SiMMs package represents a breakthrough in high-power diode-array packaging technology enabling us to scale the output of 2D diode arrays to 100 kW or larger with extremely high brightness.

—Ray Beach and Barry Freitas



Laser Science & Technology

Dr. Lloyd A. Hackel, Program Leader

UCRL-TB-136126-01-12

A 10-kW Solid-State Heat-Capacity Laser System Installed at HELSTF, White Sands Missile Range

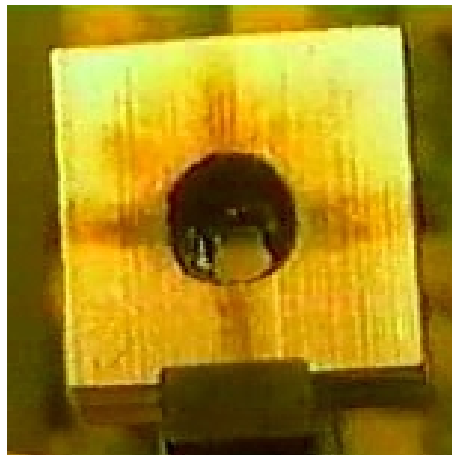
Under the support of the U.S. Army's Space and Missile Defense Command, and in collaboration with industrial partners (Raytheon, General Atomics, Northrup/Grumman Poly-Scientific, PEI, Armstrong Laser Technology, and others), LS&T is developing high-average-power (100-kW-class) heat-capacity laser technology for applications in tactical short-range air defense missions. The ultimate vision is an electrically powered, solid-state weapon that can be deployed on a hybrid electric vehicle.

To establish a solid technical basis for the heat-capacity laser operation, and to support development of an adaptive resonator, we have built a 10-kW prototype (nine-disk Nd:glass laser pumped by flashlamps). During the summer of 2001, this laser (see photo below) was delivered to the Army's High Energy Laser Systems Test Facility (HELSTF) at White Sands Missile Range to support material interaction testing.

On August 31, 2001, our milestone of 10-kW average power for 10 sec



The 10-kW laser system installed at HELSTF to support material interaction testing.



A 1-in.-thick aluminum target after a 2-sec laser burst produced a hole through it.

was exceeded when we obtained an average energy/pulse of 640 J. With the 20-Hz repetition rate, this resulted in an average power approaching 13 kW during the 10-sec burst.

On September 28, 2001, a ribbon-cutting ceremony attended by a large number of media reporters as well as high-ranking Army officials was held to commemorate the delivery of the laser.

During the ribbon-cutting ceremony, the laser was fired at a 1-in.-thick aluminum target. The photo at top of column shows the target at the end of a 5-sec burst. The hole produced by the focused laser beam penetrated the 1-in. thickness in 2 sec.

The laser will remain at White Sands where it will be used for laser/target interaction experiments until early summer of 2002. At that time, the laser will be brought back to Livermore so that a new deformable mirror may be installed.

Currently, the laser is operating with a stable resonator which is ideally suited to the target interaction experiments. A beam quality of approximately $3.5\times$ the diffraction limit has been demonstrated with an unstable resonator with no deformable

mirror correction. With the new deformable mirror and an unstable resonator, we expect to achieve the desired goal of $2\times$ the diffraction limit over the entire 10-sec run time. The beam footprint of the 10-kW laser is roughly square with a $6-\times 6.5$ -mm spot on the target.

Future plans call for a 100-kW-class, diode-pumped, solid-state laser utilizing neodymium-doped gadolinium gallium garnet (Nd:GGG) crystalline laser media for better thermal characteristics and operating efficiency. With the support of LS&T Advanced Lasers and Component, we have recently completed the



An actual 1:1 scale model of a 100-kW laser system installed on a hybrid electric HMMWV.

fabrication and testing of a 42-kW laser-diode array for pumping of Nd:GGG slabs. We will demonstrate a small-scale Nd:GGG heat-capacity laser at 200 Hz in late 2002 and replicate as closely as possible features that would be found in a fieldable unit (see photo above). For example, prime power for the laser will be provided by a bank of Li-ion batteries.

We plan to complete three-slab heat-capacity laser fabrication and testing in 2003. The scheduled completion of the 100-kW system could be as early as 2005, depending on continuing funding support.

— Mark Rotter and
C. Brent Dane